ZW2.1 Microstructure analysis and microphysical deformation mechanisms, before and after deformation experiments by

by MaP

Version: 240410

10.04.2010

by

5.1.2.e

With contributions from: 5.1.2.e

[1]MaP Microstructure and Pores GmbH

[2]**Geo**Structures

approved/reviewed by

5.1.2.e

[3]smartTectonics [4]Brouard Consulting

Comment by Joyce Schmatz, March 2024

The completion of this work involved a close partnership between MaP and Geostructures. Unfortunately, Prof. Dr. Janos L. Urai passed away on May 28, 2023, while the ongoing experimental work discussed in this report was still in progress. A significant portion of the microstructure interpretation relies on conversations I had with Janos, and I want to express my gratitude for his substantial contribution to this research.

Inhaltsverzeichnis

1 Summary

Three pre-tests and twelve full creep tests conducted on Zuidwending samples in IfG's laboratories in Leipzig were examined through microstructural analysis. The primary aim was to bridge the gap in understanding the microstructure under different stress conditions, crucial for extrapolating laboratory results to real-world scenarios. The experiments simulated salt behaviour in proximity to cavern walls under varying stresses during operation and abandonment. Notably, brine was introduced to investigate its effects on salt deformation under cavern pressure conditions. Pre-tests determined conditions for achieving non-dilatant deformation, while full creep tests explored strain behaviour at lower stresses.

Microstructural analysis revealed a complex composition of Zuidwending salt, characterized by mega-grains of halite, a fine-grained halite matrix, and layers of anhydrite. Dynamic recrystallization, pressure solution creep, and dislocation creep were identified as the dominant deformation mechanisms, with grain size influencing strain rate significantly in the natural tectonite.

Post pre-test deformation, microstructures reveal incipient dynamic recrystallization, subtly altering the original bimodal grain size distribution. The overall texture of tectonically deformed salt remains unchanged. The creep tests induced grain size reduction and structural changes, particularly in the matrix halite and the mega-grains, attributed to fluid-assisted grain boundary migration recrystallization. Second-phase impurities, such as anhydrite, acted as pinning sites for migrating grain boundaries and influenced grain size. In the case of dominant pressure solution creep, the reduced grain size as a result of the stress-strain conditions at the cavern wall after plugging and abandonment would lead to significantly higher strain rates compared to initial grain size creep rates or dominant dislocation creep deformation.

Despite extensive microstructural analysis, correlations between microstructural parameters and creep rates were found to be weak. This is likely attributed to the inherent variability of salt, the limited number of data points, and the presence of overlying microstructures that preserved successive load steps. However, discernible trends suggest that grain size and second-phase content do have an influence on strain rates, particularly within the pressure solution creep regime.

For future studies, it is advisable to conduct identical tests on a series of twin samples (within the constraints of the natural salt's heterogeneity). Furthermore, ex-situ microstructural analysis should be performed after each individual load step, ideally following longer waiting times to achieve quasi-steady-state conditions, especially in low differential stress regimes. This approach could facilitate the derivation of parameters to be more directly incorporated into constitutive equations.

This study enhances our understanding of salt behaviour under various stress conditions. It also examines the interplay between microstructural evolution and creep behaviour in salt, laying the groundwork for more accurate modelling and prediction of salt behaviour in proximity to cavern walls during operation and abandonment.

2 Laboratory creep tests on Zuidwending domal salt

In this work package, we study the mechanical characteristics and microstructural changes observed in a series of laboratory experiments. These include three pre-tests and twelve full creep tests conducted on Zuidwending samples in the laboratories of IfG in Leipzig. The experiments were focused on natural salt, a context rarely combined with conventional materials science investigations of microstructure and microchemistry, as indicated in the existing literature (Spiers et al., 1986[1], KEM-17[2] report). Consequently, extrapolating results to stresses lower than those measured in the laboratory is often judged unreliable. The primary objective of this work package is to address this gap characterizing the microstructure and combine the results with the results from the laboratory. It's noteworthy that a detailed presentation of the measurements can be found in the progress report by IfG.

The creep tests aim to enhance our understanding of salt in close proximity to the cavern wall. In this scenario, the rock is in contact with brine, and the salt undergoes varying levels of differential stress during cavern operation, followed by a decrease in stress and potentially permeation by brine during cavern abandonment. An unusual aspect of the experiments involves introducing a small amount of brine to the jacket. This serves two purposes: firstly, to replenish any evaporated brine from the core due to damage (resulting in microcracking) during coring, storage, and sample preparation. This is based on the recognition that small amounts of brine are always present in salt, and it significantly influences grain-boundary-related deformation mechanisms and processes such as recrystallization and pressure solution. Secondly, this addition helps investigate the deformation of rock salt near the (wet) cavern wall, challenging current numerical models assuming non-dilatant deformation under cavern pressure conditions.

The initial set of experiments, referred to as pre-tests, was designed to determine conditions for achieving non-dilatant deformation to about 20% strain in approximately 2 days at a constant strain rate, simulating cavern operation. The temperature was elevated to 100 ºC to expedite the tests. These pre-tests were used to design the conditions for the subsequent long-term tests: The first step of the full creep tests aimed for an axial strain of around 20%, followed by a series of creep steps at constant differential stresses much lower than the initial one. A total of 11 successful experiments were conducted in two batches: in the first batch of 6 samples were subjected to decreasing differential stress steps of 21.5, 10, 5, 4, 3, and 2 MPa. In the second batch, 5 successful tests were conducted at decreasing load steps with differential stresses of 28, 10, 5, 4, and 3 MPa. It is important to note that not all load steps were undertaken for all samples, and additional details can be found in the IfG report.

Interpreting the stress-strain results of the low-stress steps poses challenges due to small total strains in each step and significant measurement errors in axial displacements, compounded by variations in temperature, air pressure, and humidity in the laboratory. After the passing of Prof. Dr. Janos L. Urai, Dr. Richard Bakker from Nobian conducted the post-processing of the creep-test data, providing processed strain rates for the various load steps. Plotting inferred strain rates against differential stress for each load-step (Figure 1) reveals a reasonably consistent pattern, with variation in strain rates at the same differential stress among samples approximately fivefold. There is also a noticeable deviation toward faster creep than predicted by dislocation creep alone, aligning with the observed reduction in grainsize which is discussed later in this report. These data are integrated into work packages ZW2.5 and ZW2.6 to derive the most accurate creep law for the Zuidwending salt.

[1] *https://doi.org/10.1144/GSL.SP.1990.054.01.2*

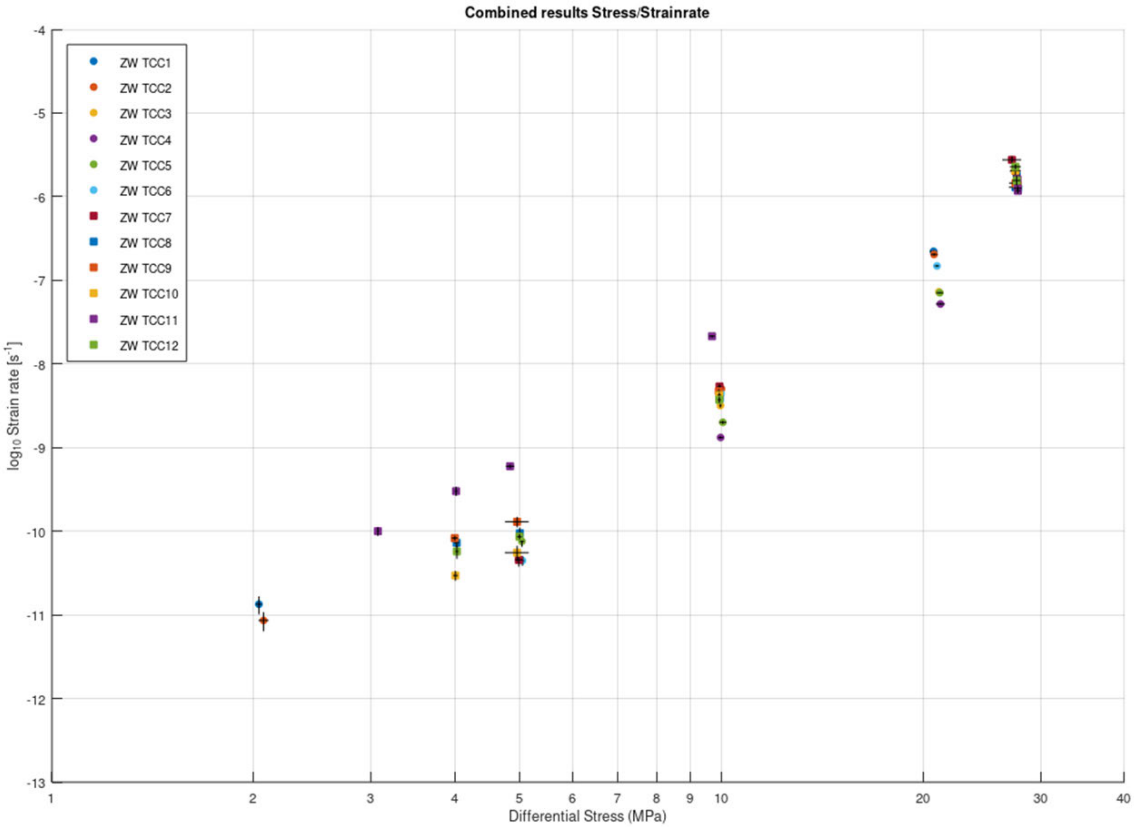

Figure 1. IfG creep tests combined processed results.

3 Summary of the microstructural investigations on Zuidwending domal salt in the initial state

The rock salt examined originates from 'Kristallbrockensalz' a renowned salt tectonite located in Zechstein II characterized by subvertical layering within the salt dome. These core sections span various stratigraphic units and extend approximately 1750 meters in depth.

In work package ZW1.2, microstructural investigations reveal three key components in Zuidwending salt: first, mega-grains of Halite, reaching decimetre lengths and up to 2 centimetres in thickness; second, a fine-grained Halite matrix; and third, thin layers of fine-grained Anhydrite folded and boudinaged, measuring a few millimetres in thickness. The mega-grains align subparallel to the bedding, while the Halite matrix constitutes a variable portion of the rock. Notably, we observed closely packed, impermeable grain boundaries hosting equilibrated micropore arrays of fluid inclusions within the halite fraction. Some grain boundaries showed dilation due to core damage. The average 2D median grain size (equivalent diameter), measured across 30 thin section samples, is 1.2 mm (with a standard deviation of 2.4 mm). Additionally, the average content of insoluble second phases was found to be 5.0 Vol.% in litho-class F, 5.8 Vol.% in litho-class G, and 17.7 Vol.% in litho-class H (defined in ZW1.1). Subgrain size piezometry suggests exposure to a maximum differential stress ranging between 1.8 to 2.3 MPa.

The presence subgrains in mega-grains (Kristallbrocken) indicates internal deformation via dislocation creep. The matrix halite underwent deformation through combined dislocation and pressure solution creep, alongside dynamic recrystallization. The rheological behaviour of Zuidwending salt is interpreted as a combination of these two deformation mechanisms, with the strain rate significantly influenced by the local distribution of mega-grains. The fine-grained matrix salt exhibits weaker properties compared to mega-grains due to differing dominant deformation mechanisms. This finding

aligns with microphysical models illustrating the substantial influence of grain size on strain rate, particularly at low differential stress levels, offering evidence for the prevalence of pressure solution creep in rock salt under stresses of a few MPa.

The sample material covers the following litho-classes: Lithoclass F, almost pure salt with thin Anhydrite layers and Halite mega-grains, litho-class G: Minor amount of mega-grains (average of core and slab fraction <25%), and litho-class H: salt with anhydrite dust, mega-grains, and a mylonitic fabric (Table 1, Figure 2).

Table 1 Core Piece well information and litho-class

Well_Core_box_depth [m]	*Litho-class ZW1.1*	*MaP ID ZW1.2*	*MaP ID ZW2.1*	*IfG ID*	*batch creep-test*
ZW A1A_2_2_452.62	F	ZW_MaP_16	ZW_MaP_35_d	TCC1	1st batch
ZW A1A_4_7_959.2	F	ZW_MaP_13	ZW_MaP_39_d	TCC2	1st batch
ZW A2A_7_9_1467	G(F)	ZW_MaP_09	ZW_MaP_17_pre	Pre-1	Pre-test
ZW A2B_1_2_650.8	G(F)	ZW_MaP_14	ZW_MaP_44_d	TCC7	2nd batch
ZW A3A_1_2_591.9	H	ZW_MaP_15	ZW_MaP_45_d	TCC8	2nd batch
ZW A3A_2_1_991	H	ZW_MaP_21	ZW_MaP_36_d	TCC4	1st batch
ZW A3A_6_5_1444.5	H	ZW_MaP_10	ZW_MaP_46_d	TCC9	2nd batch
ZW A4A_5_10_1028	G	ZW_MaP_12	ZW_MaP_34_d	TCC5	1st batch
ZW A5A_6_9_1190.47	H	ZW_MaP_11	ZW_MAP_49_d	TCC12	2nd batch
ZW A5A ST01 _1_5_1503.26	G	ZW_MaP_07	ZW_MaP_18_pre	Pre-2	Pre-test
ZW A7B_2_15_1469.27	G	ZW_MaP_08	ZW_MaP_47_d	TCC10	2nd batch
ZW A8A_2_10_542.23	G	ZW_MaP_02_g	ZW_MaP_38_d	TCC6	1st batch
ZW KNZ-8_1_10_242.7	F	ZW_MaP_01_g	ZW_MaP_48_d	TCC11	2nd batch
ZW KNZ-8_1_10_242.7	F	ZW_MaP_01_g	ZW_MaP_19_pre	Pre-3	Pre-test
ZW KNZ-8_13_8_1627.58	H	ZW_MaP_03_g	ZW_MaP_37_d	TCC3	1st batch

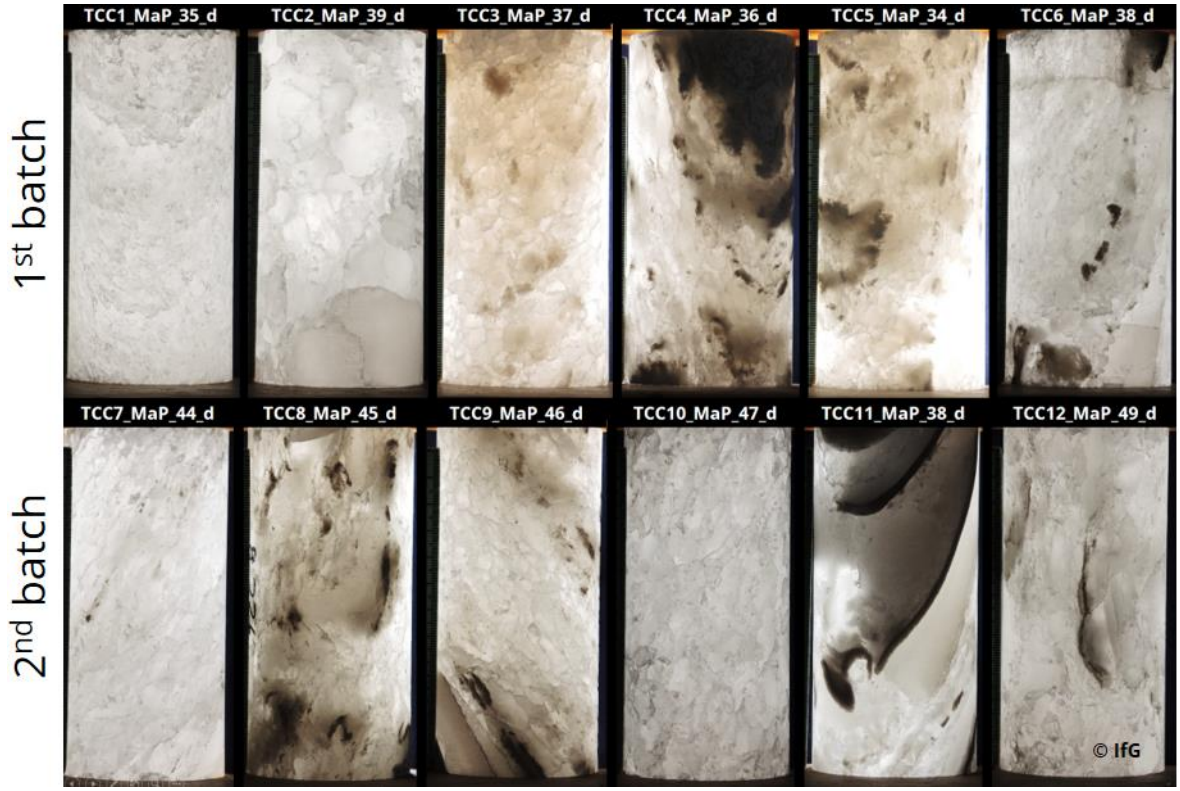

Figure 2. Transmitted light photographs of core pieces prepared at IfG for creep testing. The photos were prepared by IfG. The heading indicates the IfG test ID (e.g., TCC1) and the ID used by MaP in the ZW1.1-, and ZW1.2-reports, and this report. See the Appendix A for the IfG core piece photographs before and after testing.

4 Microstructural analysis and microphysical deformation mechanisms

4.1 Introduction

The aim of this work package is the description and analysis of the of selected sample material from completed deformation experiments (work package ZW2.2) regarding the microstructural properties with special emphasis on the microstructural processes and deformation mechanisms recorded in the microstructure. Special attention will be paid to characteristics that influence the microphysical properties of the salt, such as the grain size and the impurity content. We report on the microstructural properties of the samples deformed in the laboratory, as determined by state-of-the-art microanalytical imaging technologies in combination with image analysis and bulk measurements. A qualitative assessment of the deformation mechanisms such as dislocation creep, pressure-solution creep, as well as a description of features that influence the salts' rheology, such as grain boundary structure, grain boundary fluid distribution, and impurity pinning are part of in the report. Furthermore, we provide a comparison on the microstructural processes of the tectonically-deformed samples with the lab--deformed samples (pre-tests and full creep tests). The results of the microstructural analysis are integrated with - and in discussed in the context to the laboratory tests.

The observational and theoretical background on which this interpretation is based is reviewed extensively in the KEM-17 report[2] and will not be repeated here, so in this report we do not include extensive referencing but rather refer to KEM-17.

[2] *https://www.sodm.nl/documenten/rapporten/2020/02/11/onderzoek-langetermijnrisicos-afsluiten-zoutcavernes*

4.2 Methods

We utilized advanced microanalytical tools to examine the microstructure across scales ranging from centimetres to nanometres. Initial examination involved transmitted and reflected light photographs of core pieces both before and after deformation. Additionally, an analysis of slabs prepared in the centre of deformed core pieces and their respective twin core pieces (as detailed in ZW1.1 report), oriented perpendicular to the bedding, allowed us to evaluate the spatial distribution of phases: halite matrix grains, halite mega-grains, and anhydrite. It is important to note that the phase referred to as anhydrite is a mixture of anhydrite with polyhalite (refer to ZW1.1 for a comprehensive description of litho-classes and phase composition). The overall grain-scale microstructure was examined using transmitted light scans of thick sections approximately 1 mm in thickness.

Grain- and subgrain sizes were measured from thin section micrographs captured in reflected light following surface etching using semi-automated image analysis (refer to ZW1.2 for a comprehensive description of the microanalysis). Transmitted, plane-polarized light micrographs were employed to investigate grain boundary fluid morphology, second-phase impurities, and microcracks. SEM-EDS analysis on thin sections was employed to assess second-phase impurities, while BIB (Broad Ion Beam) surface preparation facilitated a high-resolution examination of grain boundary structure and porosity in the SEM (Scanning Electron Microscope). High-resolution SEM on halite polycrystals was used to investigate grain surface morphology and surface imprints of fluid inclusion arrays.

4.3 Results and Discussion

4.3.1 Microstructural processes

4.3.1.1 Pre-tests

The initial composition of Zuidwending salt exhibits a distinctive texture with halite mega-grains embedded within a matrix of fine- to coarse-grained polycrystalline halite. The transition from the matrix to mega-grains is marked by elongated, straight grain boundary segments in the mega-grains, often bordered by thin anhydrite bands measuring a few millimetres (Figure 3, sample Pre-1_MaP_17_d). Mega-grain boundaries not adjacent to anhydrite bands may exhibit irregularities, signifying the interface of tectonically driven recrystallization in the matrix halite (refer to the ZW1.2 report for detailed information). Samples, however, were pre-selected to represent rather the matrix grain facies in order to allow studying the creep-behaviour in laboratory time scales, thus mega-grain occurrence is rare throughout the tested sample material. Despite undergoing a short pre-test at high deviatoric stress (Figure 3, and a contrasting comparison in the Appendix A using the initial twin sample), the overall texture is maintained. However, microstructures post pre-test deformation reveal incipient dynamic recrystallization, subtly altering the originally bimodal grain size distribution (refer to the KEM-17 report microstructure). This alteration introduces a class of very small, newly recrystallized grains (Figure 4). Dynamic recrystallization is a process observed in minerals subjected to high strain conditions, involving grain size reduction and restructuring. The initial phase of dynamic recrystallization is nucleation, wherein new crystals (grains) form within the rock (Figure 5). Following nucleation, these newly formed grains undergo growth, enlarging particularly in areas of intense deformation. The growth process is facilitated by the migration of grain boundaries and material absorption from adjacent grains. As the process continues, the rock undergoes recrystallization, replacing the original crystal structure with a finer grain arrangement. The finer grain size observed is a distinct feature of dynamic recrystallization, often linked to heightened ductility and deformation accommodation facilitated by pressure solution creep within the rock. However, the analysis of grain types, as depicted in Figure 4, underscores that the matrix grains underwent partial replacement by newly recrystallized grains, accounting for approximately 25 area% in the three pre-tests. Nucleation and growth manifest at diverse locations within the grain fabric, primarily at grain boundaries but also

within the grains themselves. Mega-grains, initially characterized by numerous second-phase inclusions, undergo a transformation into clear, cubic grains, predominantly occurring at the grain boundaries through dynamic recrystallization. Nevertheless, as highlighted earlier, the mega-grains, overall, experience only minor or incipient effects from dynamic recrystallization during the pre-test.

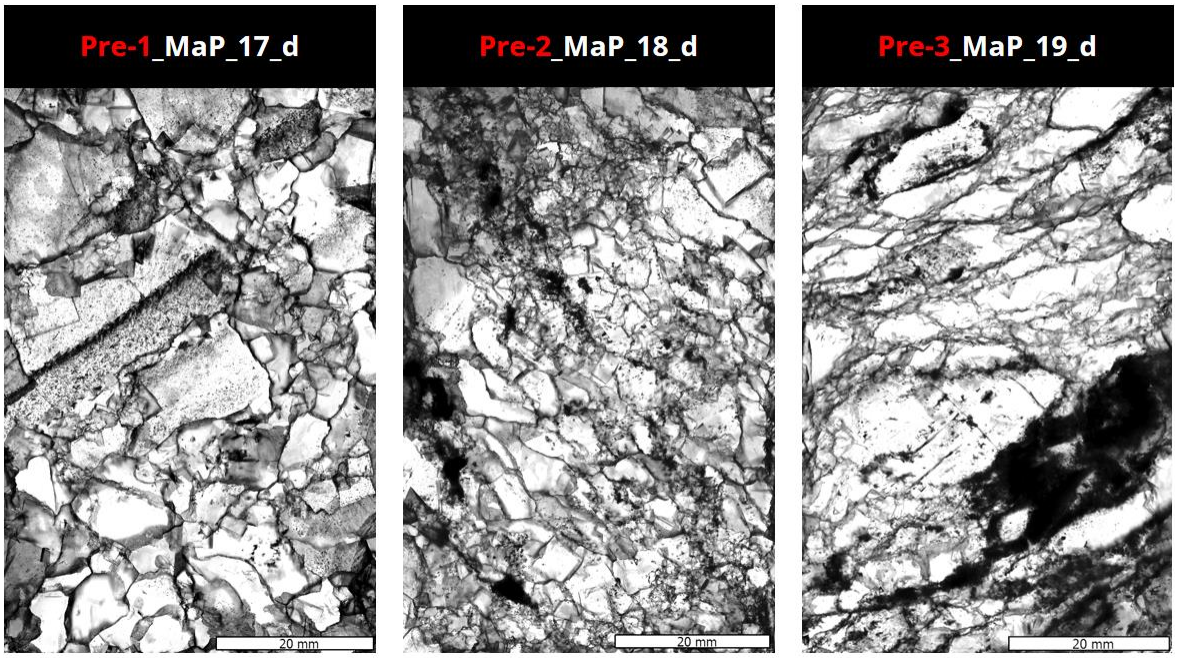

Figure 3. Transmitted light flatbed scans reveal the structure of the pre-tested samples, namely Pre-1_MaP_17_d, Pre-2_MP_18_d, and Pre-3_MaP_19_d. In these samples, matrix grains exhibit partial recrystallization, and the grain boundaries are tight, making them often imperceptible. Mega-grains, for the most part, remain intact, although they undergo dynamic recrystallization at the grain boundaries and occasionally within the grains themselves.

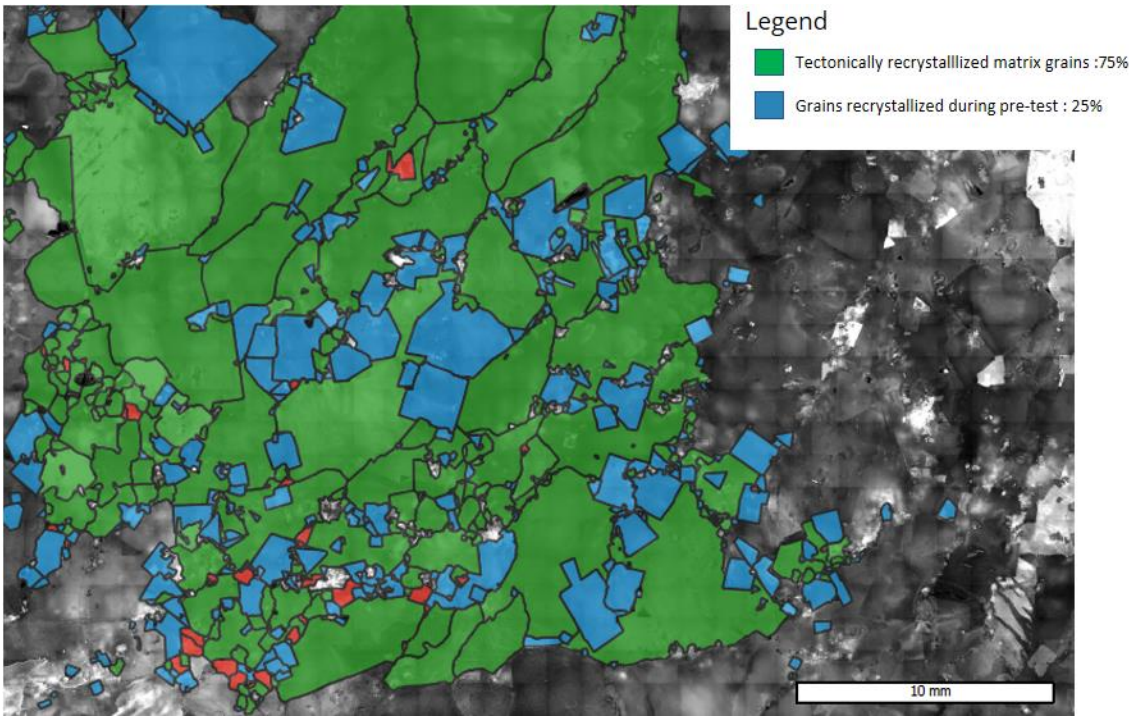

Figure 4. Interpreted grain size map of the pre-tested sample Pre-2_MaP_18_d_MaP_07 reveals the proportion of newly recrystallized grains formed during the pre-testing in comparison to the preserved tectonically-driven recrystallized matrix grains. Around 25 area% of the matrix halite recrystallized during the pre-test.

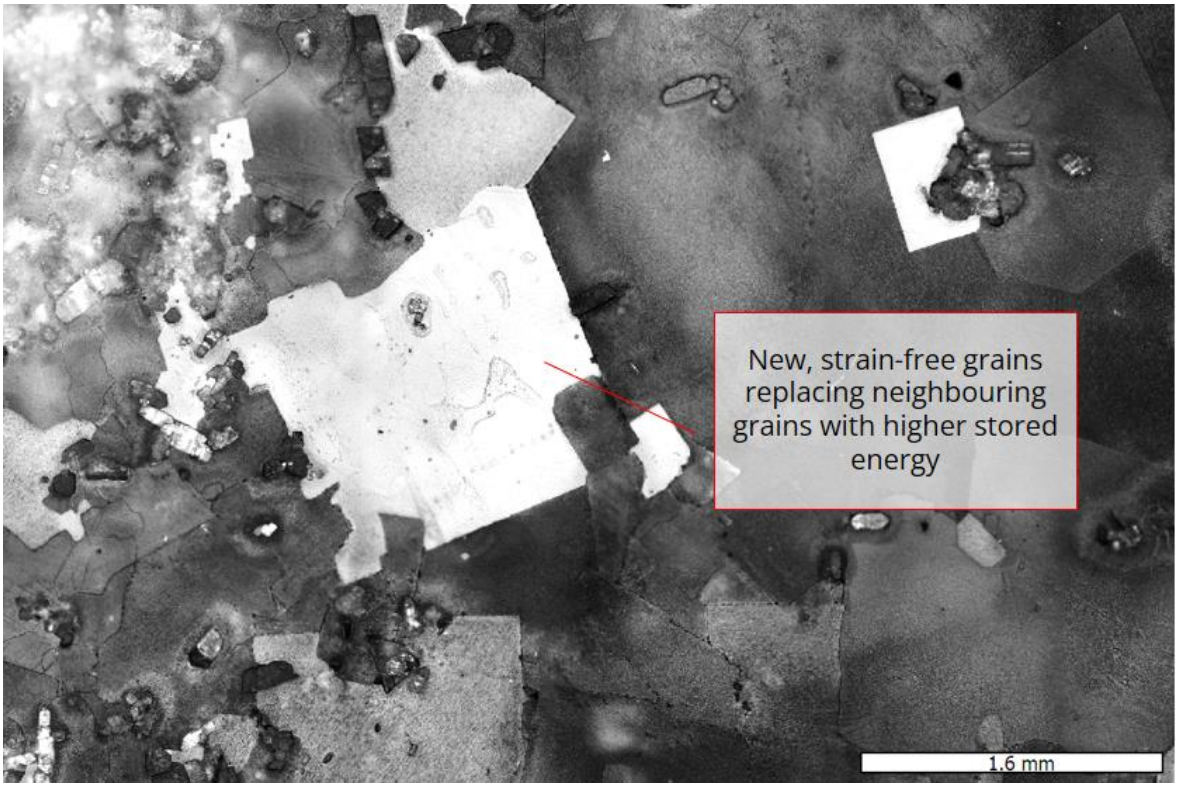

Figure 5. Pre-test reflected light micrograph. Grains with high dislocation density were replaced by "new" grains by nucleation and nucleus growth and strain-induced grain boundary migration. "New", recrystallized grain growing into adjacent grain of higher energy and removes the deformed microstructure of the consumed grain.

4.3.1.2 Creep tests – texture

In contrast to the initial samples and those deformed in pre-tests, specimens subjected to creep tests under high deviatoric stress exhibit notable alterations in their initial texture. Notably, there is an overall reduction in matrix grain size (Figure 6 and Figure 7), accompanied by a discernible decrease in the grain size of mega-grains (Figure 6, refer to the Appendix A, sections TCC2, TCC3, TCC9, and TCC12 for a juxtaposition of transmitted light thin section images of the initial samples with images of the creep-tested samples). In most cases the original arrangement of mega-grains within the creep-tested samples cannot be identified. Mega-grains located at the bottom or top of the deformed core-pieces are preserved in samples TCC7_MaP_44_d and TCC9_MaP_46_d, pointing to a possibly non-uniform strain pattern within the deformed core piece.

The restructuring of mega-grains is ascribed to the progressive strain-induced distortion of the crystal lattice, leading to dynamic grain boundary migration recrystallization. Notably, the internal structure of mega-grains, characterized by numerous second-phase inclusions, does not appear significantly affected by this process. Depending on the ratio of grain boundary velocity with the second phase mobility, low-mobility second phases can be passed by migrating grain boundaries without significant alteration (e.g., Schmatz and Urai, 2010[3]; Schmatz and Urai, 2011[4]). In contrast to regions adjacent to matrix grains, where mobile grain boundaries erase the crystal's original lattice while incorporating fluid and solid inclusions through a dissolution-precipitation process—resulting in clear, strain-free grains.

[3] *https://onlinelibrary.wiley.com/doi/10.1111/j.1525-1314.2009.00849.x*

[4] *https://www.sciencedirect.com/science/article/abs/pii/S0191814110002567*

Figure 8 illustrates a scenario exemplifying the transformation of the halite matrix-grain texture. The grain size has undergone a substantial reduction through the nucleation and growth of small, frequently equiaxed grains. These newly formed grains effectively obscure the original texture, initially characterized by elongated grains with interlobate grain boundaries (see the Appendix A for reflected light micrographs showing the initial texture of the twin samples juxtaposed with reflected light micrographs showing the texture of the creep-tested samples). The tectonically deformed samples showcase visually recrystallized, strain-free grains, often retaining remnants of older grains with subgrains in between. The grain boundaries are decorated with numerous fluid inclusions and can exhibit dilation, likely influenced by storage conditions. Additionally, the grain boundaries form 120° triple junctions and vary from straight to interlobate. In samples subjected to creep tests, the presence of small, strain-free recrystallized grains with a predominantly equiaxial shape was noted (Figure 7 and Figure 8a). Additionally, there are grains with lobate grain boundaries growing into structures that display visible substructuring with small subgrains and/or dense slip bands (Figure 8b-g). These observations strongly suggest the ongoing occurrence of dynamic recrystallization (grain boundary migration recrystallization) as a dominant microstructural process.

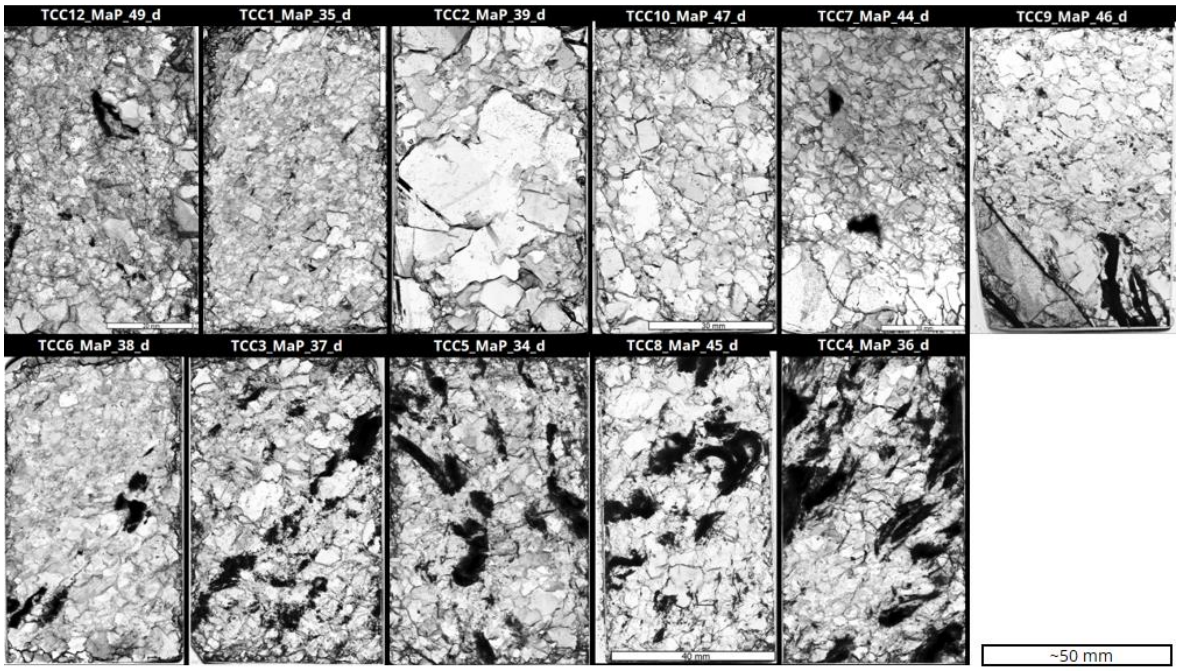

Figure 6. Transmitted light scans of the creep-tested samples reveal the overall texture, featuring areas of small, recrystallized matrix grains, and mega-grains that underwent varying degrees of recrystallization. The dark, in 1 mm thick sections optically inert, Anhydrite bands and inclusions are bent and ruptured. Upper row left to right, then lower row left to right the samples were sorted by overall decreasing strain rates.

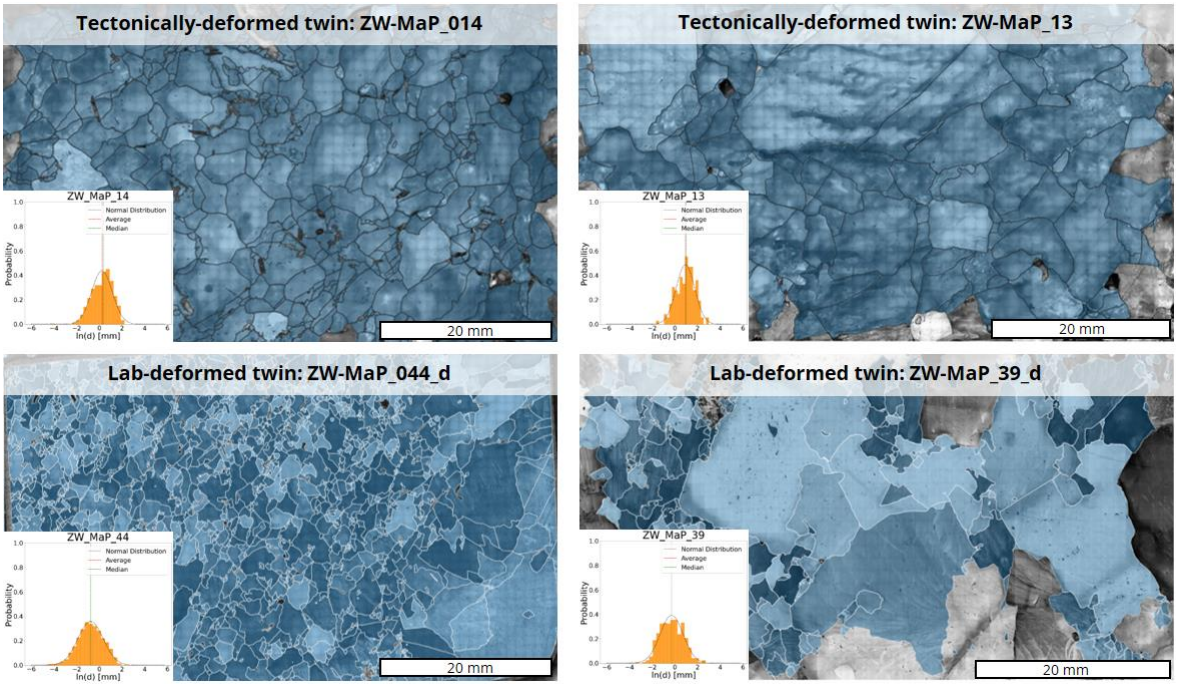

Figure 7. The grain size of the creep-tested sample is diminished by a factor of 3.1 for the finer-grained sample ZW_MaP_44_d (left) and by a factor of 3.6 for the coarser-grained sample ZW_MaP_39_d (right). Previously elongated grains with straight to interlobate grain boundaries exhibit epi-axial shape, ranging from straight for the very small recrystallized grains to lobate for the larger grains, indicative of dynamic recrystallization.

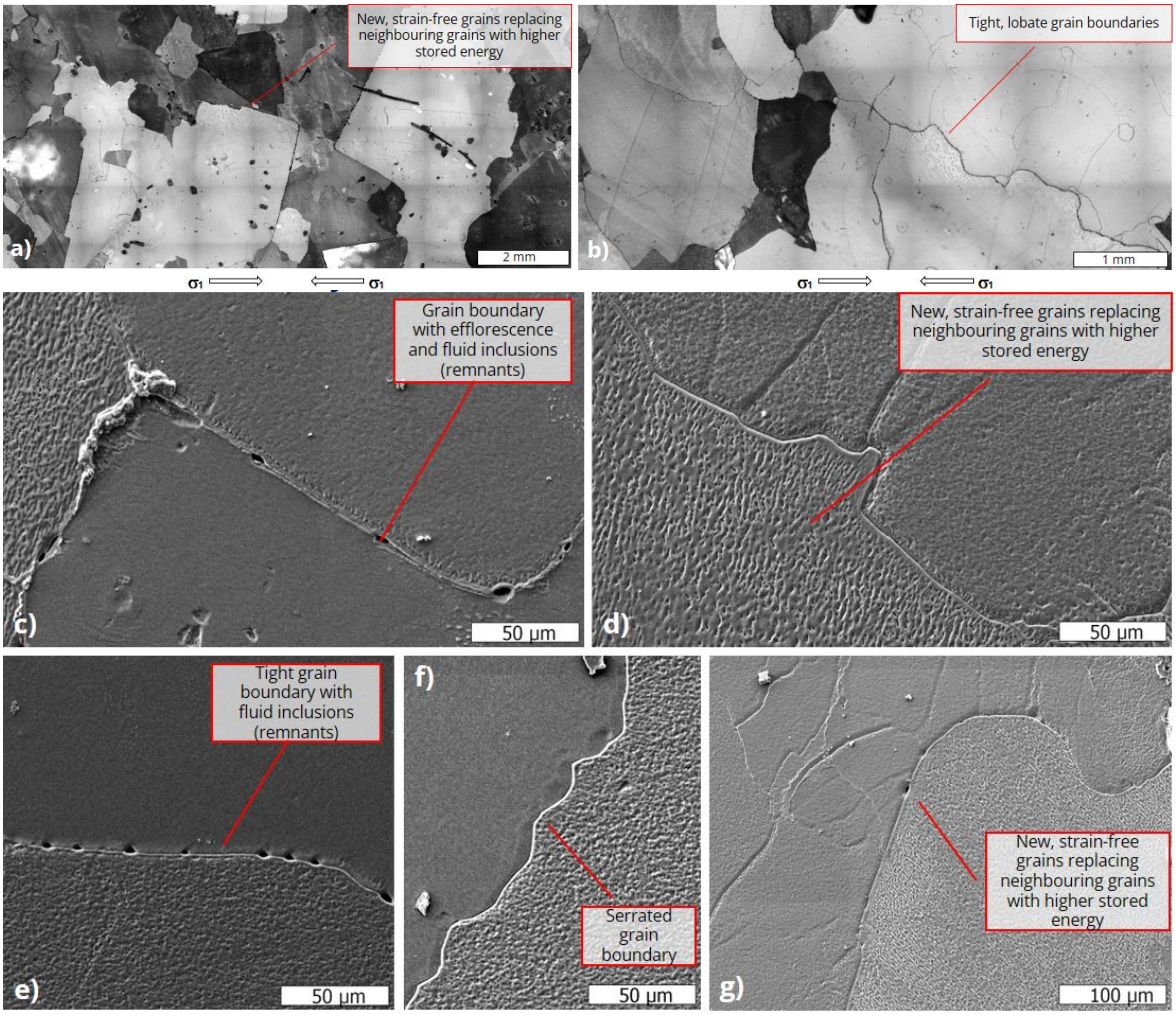

Figure 8. a) and b) reflected micrographs showing the texture of the matrix after the creep test. c)-g) secondary electron images of etched thin section. See text for details and the Appendix A for further examples.

4.3.1.3 Creep tests - grain boundary processes

The examination of grain boundaries following creep tests reveals a spectrum of structural features associated with the varied stress conditions during the tests. In contrast to the frequent presence of grain boundary fluid inclusions in the tectonically-deformed samples, grain boundary fluids are less commonly observed in the optical microscope (refer to Figure 9) in the creep-tested samples. Grain boundaries that still exhibit fluid inclusions with sizes in the range of a few tens of µm (and are thus visible in the optical microscope) are considered remnants of the initial structure. Some of these boundaries may become mobile during creep but are pinned by the fluid inclusions (refer to the Appendix A, e.g., samples TCC1, TCC8, TCC10, and TCC12), resulting in the formation of bulges. These bulges can serve as preferred sites for the nucleation and growth of new grains, and these structures are thought to form during dynamic recrystallization. Efflorescence observed along grain boundaries is thought to indicate the presence of aqueous grain boundary fluids in the creep-tested samples (Figure 9b, Schenk an Urai, 2004[5]).

The investigation of grain boundary morphology in the SEM on surfaces of polycrystals broken along the grain boundaries facilitates a comparison of the initial configuration of grain boundary fluids with the fluid inclusion pattern after the creep tests (Figure 10). As detailed in the ZW1.2 report, the initial samples feature grain boundaries decorated with regular arrays of isolated, well-equilibrated fluid inclusions. The shapes of these inclusions range from nearly spherical to elongated, sometimes

[5] *https://link.springer.com/article/10.1007/s00410-003-0522-6*

amoeboid, correlating with various lattice orientations on different surfaces. The size of fluid inclusions varies widely, from tens of nanometers to several tens of micrometers, though it was not quantified in this study. Amid the fluid inclusion imprints, remnants of solid-solid contacts are preserved in the initial samples. The grain boundaries in the creep-tested samples exhibit fewer locations with visible imprints of fluid inclusion arrays. However, grain boundaries that are decorated with imprints of fluid inclusion arrays are very similar to the initial grain boundaries with this regard. The grain boundaries of the cubic, recrystallized grains that grow into older grains with higher stored energy, visible in form of substructures such as small subgrains and dense slip bands, however, are smooth and nearly free of fluid inclusions. High-resolution SEM suggests the presence of semi-connected fluid films along these grain boundaries.

Overall, the examination of grain boundary morphology, with a focus on the distribution of fluid imprints, suggests indications of semi-connected fluid films spread on the grain surfaces of the creep-tested samples. Transparent thin aqueous fluid films may remain invisible in transmitted light microscopy due to their optical properties.

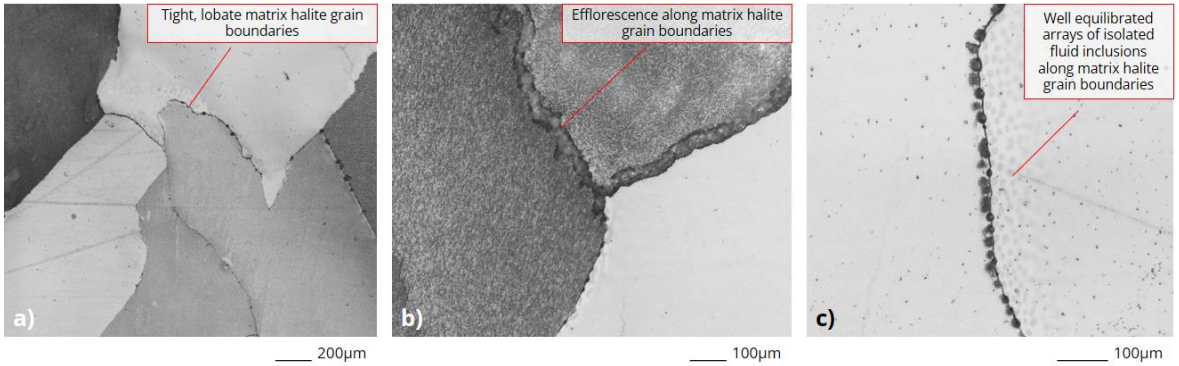

Figure 9. Reflected micrographs showing the grain boundary structure of the matrix grains after the creep test with a) tight, lobate grain boundaries, decorated with few fluid inclusions that occasionally pin the grain boundaries, b) efflorescence along grain boundaries indicating the presence of grain boundary fluids prior to sample preparation, and c) well equilibrated arrays of isolated fluid inclusions.

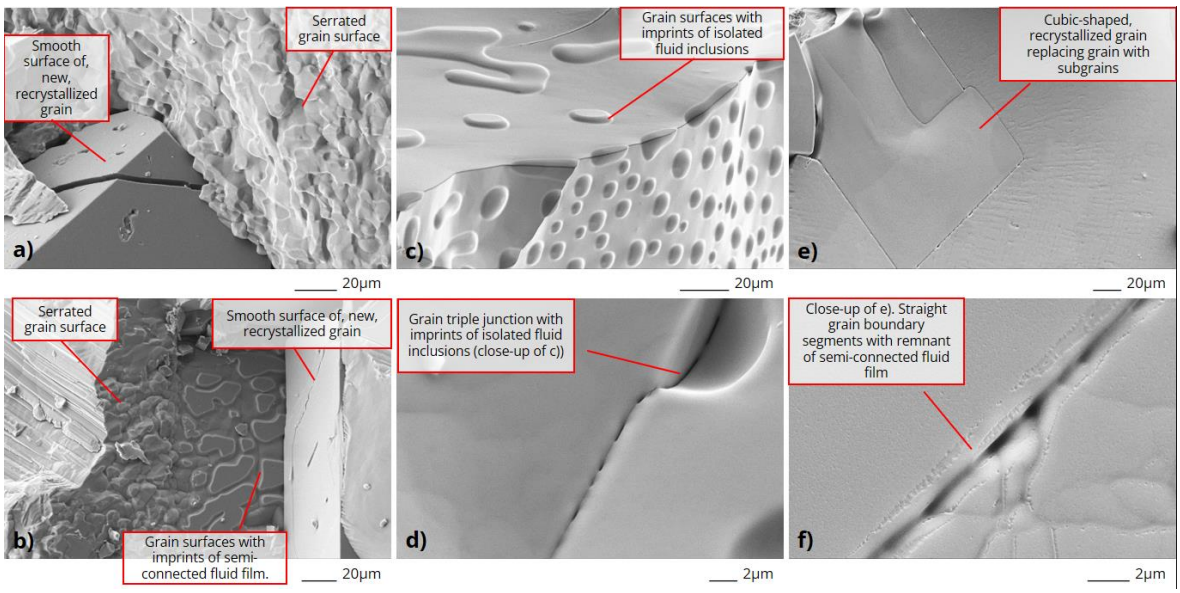

Figure 10 Secondary electron images showing the grain surfaces of the matrix grains. See text and figure annotations for details.

4.3.1.4 The role of second phase inclusions

The overall distribution of second-phase impurities in relation to the matrix grains remains largely unchanged following the creep tests. Similar to the tectonically deformed samples, anhydrite/polyhalite inclusions of the second phase persist, appearing either as fine-grained clusters or large idiomorphic grains within halite grains or enclosed within them. Notably, at grain boundaries, there is a more frequent observation of anhydrite grains pinning mobile grain boundaries (refer to the Appendix for numerous examples), a feature also visible in the tectonically deformed samples. Although grain boundary pinning may lead to a refined grain size compared to samples with minimal second-phase content, the limited occurrence of this process in both creep-tested and non-creep-tested samples suggests a minimal impact on the overall texture or grain boundary structure of the salt.

Large, idiomorphic anhydrite grains serve as strain markers and undergo deformation in a ductile-brittle fashion. Both creep-tested and tectonically deformed samples exhibit bent anhydrite grains (see Figure 11) with an inclined orientation to the maximum principal stress (top-bottom orientation in the tectonically deformed twins). Moreover, in the creep-tested samples, in contrast to tectonically deformed ones, ruptured anhydrite grains are frequently observed, often displaying boudinage structures. The edges of ruptured grains are embedded in the matrix halite, with only large, millimetre-range, idiomorphic anhydrite grains oriented perpendicular to sigma 1 with their long axis exhibiting boudinage.

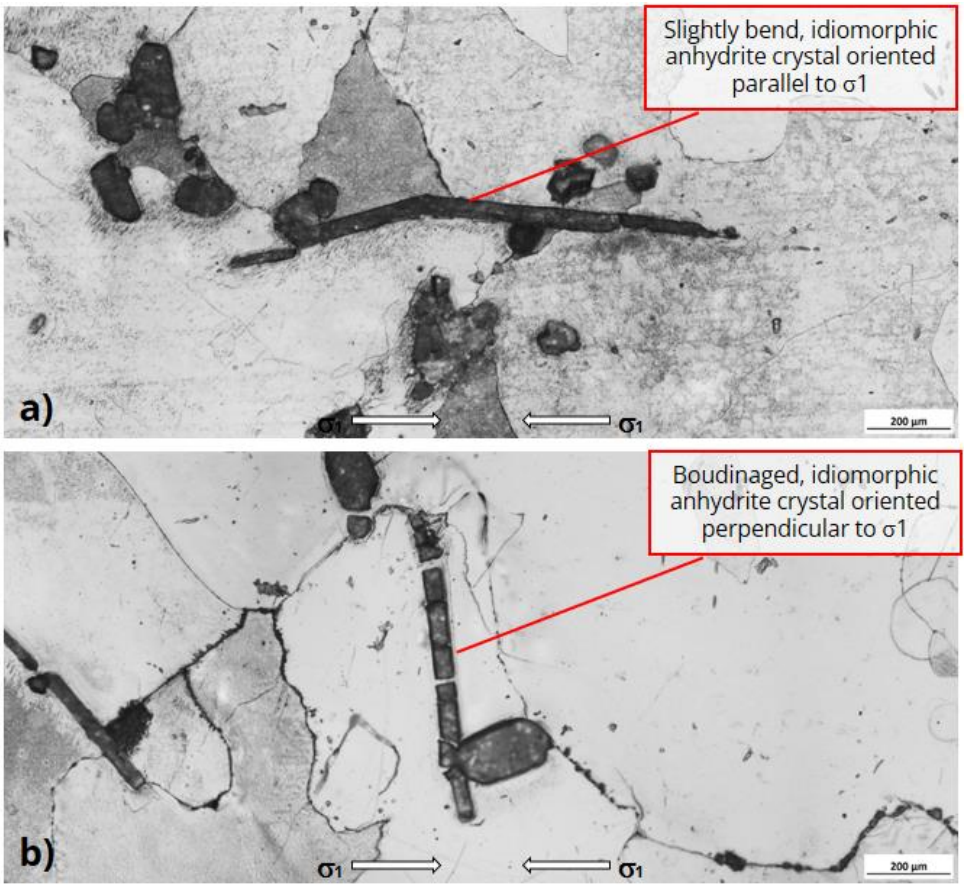

Figure 11. Reflected micrographs showing the second phase inclusions within the creep-tested samples. See text for details and the Appendix A for further examples.

4.3.2 Quantitative microstructure

4.3.2.1 Relative phase composition

Slabs, oriented perpendicular to the bedding and positioned at the center of the core pieces, were prepared from the core pieces, and segmented to identify the relative distribution of three phases: anhydrite (including polyhalite), halite mega-grains, and halite matrix grains (refer to Figure 12a). This segmentation was conducted at a relatively large scale, providing a wide field of view at low resolution. The mega-grain content varies between 0,0% and 20,8% area-wise, with an average of 8,8% for the tectonically-deformed twin samples (see Table 2).

Further, we investigated the second-phase content from the powder derived from machining the core pieces to the desired size for lab tests (Figure 12b, **Fehler! Verweisquelle konnte nicht gefunden werden.**). Refer to the ZW1.2 report for a detailed description of the method. The average second-phase (insoluble) content derived from the dissolved powder is 7.1 vol.%, and 0.9 vol.% was derived from the slab segmentation. The significant difference is related to the different types of measurement (volume vs. area) and the differences in location: the slab measurement records the second-phase content in a plane in the centre of the sample, while the powder measurement records the content within the non-preserved edges of the samples. Core pieces TCC3_MaP_37_d, TCC4_MaP_36_d, and TCC8_MaP_45_d have a relatively high second-phase content, around 16 vol.%, and core pieces TCC1_MaP_35_d, TCC2_MaP_39_d, TCC7_MaP_44_d, and TCC10_MaP_47_d have a relatively low content of second phases, around 2.5 vol.%.

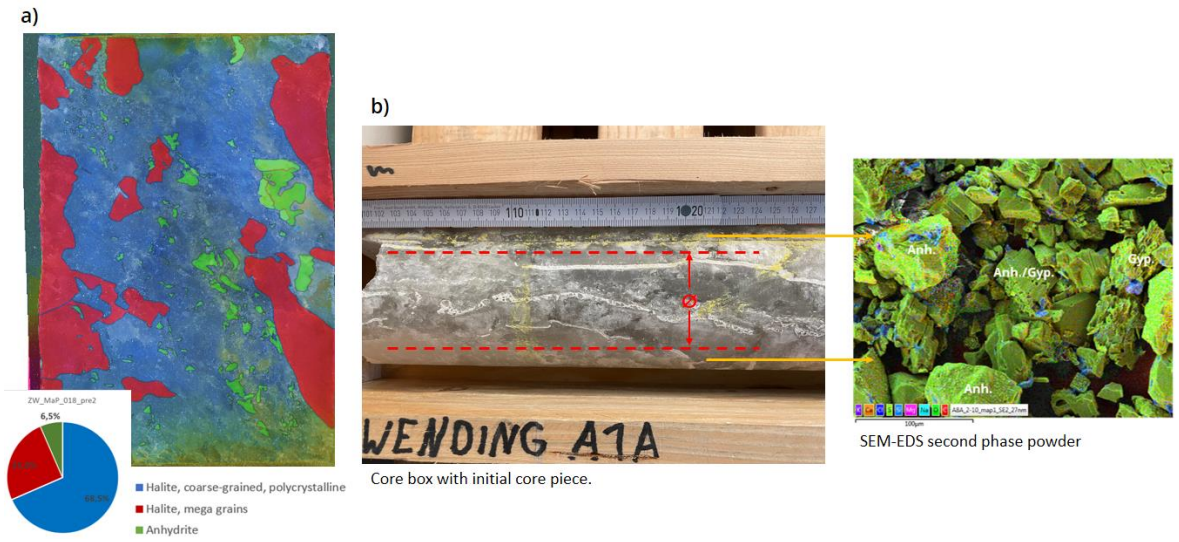

Figure 12. a) Transmitted light slab photography, accompanied by segmentation, reveals the distribution of phases, including anhydrite, halite mega-grains, and halite matrix grains. b) Core material was machined down at IfG to desired diameter for deformation/permeation test. The resulting powder was used to determine the insoluble content.

Table 2 Quantitative Microstructure

Depth [m]	Core piece ID (well_core_box)	MaP ID	Twin MaP ID (ZW1.1)	IfG lab lest ID	Median grain size [mm]	St.Dev. median grain size [mm]	Twin median grain size [mm] (ZW1.2)	Twin St.Dev. median grain size [mm]	Grain size refinement factor compared to twin	Second phase content from dissolved powder [vol.%]	Twin second phase content from slab segmentation [area%] (ZW1.1)	Twin mega-grain content from slab segmentation [area%] (ZW1.1)	Twin matrix grain content from slab segmentation (ZW1.1)
1467.8	ZW A2A_7_9	ZW_MaP_17_pre	ZW_MaP_09	TCpre1	0.41	2.73	1.47	3.61	3.6	3.3	0.3	13.3	86.4
1503.9	ZW A5A ST01_1_5	ZW_MaP_18_pre	ZW_MaP_07	TCpre2	0.33	2.71	1.35	3.68	4.1	5.3	0.2	18.8	81.0
243.3	ZWD-KNZ-8_1_10	ZW_MaP_19_pre	ZW_MaP_01_g	TCpre3	0.29	2.73	1.09	2.40	3.7	8.8	0.0	5.5	94.5
453	ZW A1A_2_2	ZW_MaP_35_d	ZW_MaP_16	TCC1	0.62	2.43	1.62	2.10	2.6	2.9	0.0	0.0	100.0
959.5	ZW A1A_4_7	ZW_MaP_39_d	ZW_MaP_13	TCC2	0.74	2.76	2.66	2.26	3.6	2.7	0.0	19.0	81.0
1627.6	ZWD-KNZ-8_13_8	ZW_MaP_37_d	ZW_MaP_03_g	TCC3	0.59	2.14	2.54	2.57	4.3	15.7	0.0	0.0	100.0
991.3	ZW A3A_2_1	ZW_MaP_36_d	ZW_MaP_21	TCC4	0.63	2.22	1.06	2.45	1.7	13.9	4.6	9.4	86.0
1028.5	ZW A4A_5_10	ZW_MaP_34_d	ZW_MaP_12	TCC5	0.41	2.28	1.25	3.33	3.0	5	4.0	8.0	88.0
543	ZW A8A_2_10	ZW_MaP_38_d	ZW_MaP_02_g	TCC6	0.68	2.24	1.27	2.55	1.9	6.4	0.3	17.2	82.5
651.4	ZW A2B_1_2	ZW_MaP_44_d	ZW_MaP_14	TCC7	0.46	3.04	1.41	2.48	3.0	2.8	0.0	0.0	100.0
592.4	ZW A3A_1_2	ZW_MaP_45_d	ZW_MaP_15	TCC8	0.39	2.85	0.93	3.22	2.4	16.9	0.3	5.9	93.8
1445.3	ZW A3A_6_5	ZW_MaP_46_d	ZW_MaP_10	TCC9	0.39	3.04	1.22	3.67	3.1	7	1.1	4.3	94.6
1469.5	ZW A7B_2_15	ZW_MaP_47_d	ZW_MaP_08	TCC10	0.46	3.21	2.02	3.50	4.4	1.6	0.0	0.0	100.0
243.3	ZWD-KNZ-8_1_10	ZW_MaP_48_d	ZW_MaP_01_g	TCC11	0.49	1.00	1.09	2.40	2.2	10.7	2.4	9.9	87.7
1190.9	ZW A5A_6_9	ZW_MAP_49_d	ZW_MAP_11	TCC12	0.30	3.26	1.48	2.47	4.9	3	0.2	20.8	79.0

4.3.2.2 Grain size and second phase impurities

4.3.2.2.1 Pre-test

As illustrated in Figure 4 and Figure 5, dynamic recrystallization initiated grain refinement in the pre-tested samples. During the pre-test conducted at 100°C with a total strain of 20%, around 25area% of the matrix grains in the pre-tested samples were replaced by new, recrystallized grains. The grain size, whether before or after the pre-test, follows a log-normal distribution (refer to Figure 13, Table 3). In this report, the grain size refinement factor is defined as the median grain size of the tectonically-deformed twin samples divided by the grain size of the creep-tested twin samples, which is on average 3.8 for the matrix grain fraction in the pre-tested samples. It's worth noting that mega-grains were only minimally affected by dynamic recrystallization and were not included in the grain size measurement due to their size exceeding the dimensions of the thin section.

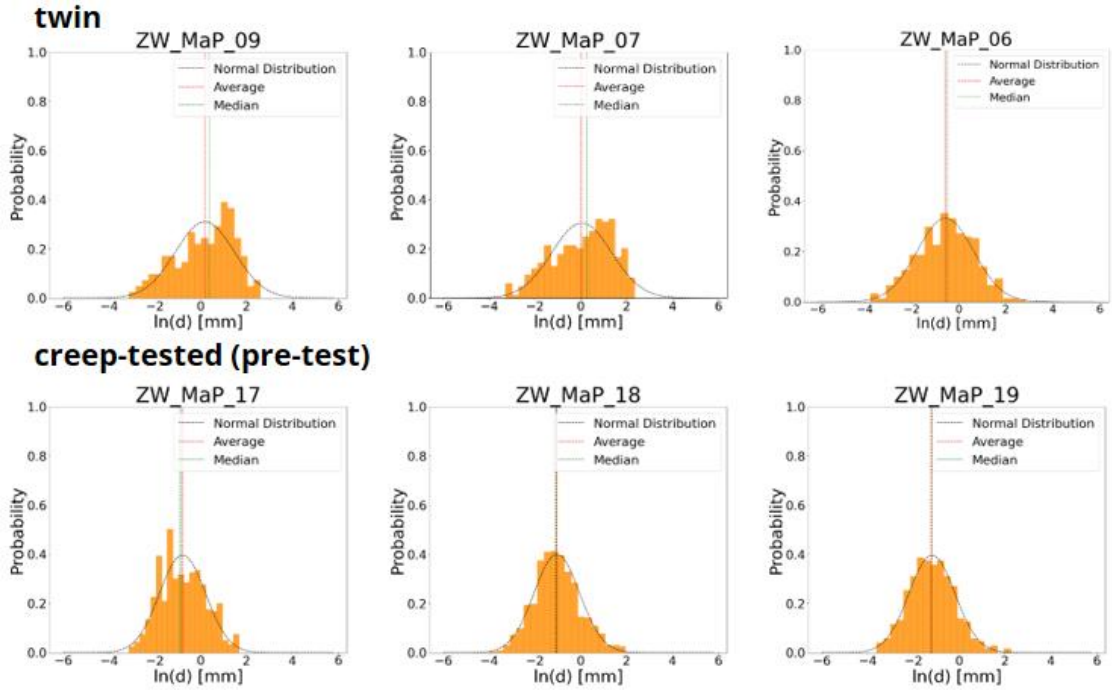

Figure 13. Histograms show the grain size distribution of the tectonically-deformed samples in the upper row, juxtaposed with the pre-tested samples in the lower row. For additional details on the grain size statistics, refer to the accompanying text, Table 2 and Table 3, and consult Appendix A for information on grain size measurements.

4.3.2.2.2 Creep tests

During the creep tests, the initial grain size measured in the tectonically deformed twin samples consistently decreased. For both the tectonically deformed samples and the lab-deformed sample, grain size follows a log-normal distribution (refer to Figure 14), with an average median grain size of 1.46 mm (n= 12, min= 0.93 mm, max= 2.66 mm, Std.Dev= 0.48 mm, see Table 3) for the tectonically-deformed twins and 0.51 mm (n=12, min=0.30 mm, max=0.76 mm, Std.Dev= 0.13 mm, see Table 2) for the creep-tested samples (refer to Table 3 for grain size statistics of the lab-deformed samples and ZW1.2 report for the statistics of the tectonically deformed samples, with a summary given in Table 2). The grain size refinement factor is on average 3.1 (n=12, min= 1.7, max= 4.9, Std.Dev= 1.0, see Table 2), indicating a significant decrease in grain size for all lab-deformed samples (refer to Figure 15a).

As shown in Figure 7 exemplifying the grain size measurement for a rather coarse-grained initial sample (TCC2_MaP_39_d) and a rather fine-grained initial sample (TCC7_MaP_44_d), the difference in grain size before and after the test is with a refinement factor of 3.6 not significantly larger for the coarse-grained samples compared to the fine-grained samples with a factor of 3.0. This observation allows the conclusion that the initial grain size is recorded in the recrystallized grain size after the creep test.

Samples were creep-tested in two batches with a different starting load step at 21.5 MPa and 28 MPa differential stress, respectively. Comparing the post-mortem grain size after completing of the creep-tests results in an average grain refinement factor of 2.6 (+/-0.9) for the first batch at the lower initial load and an average grain refinement factor of 3.6 (+/-1.2) for the second batch deformed at the higher initial load, indicating that the load history influences the recrystallized grain size (Figure 15b).

The effect of second-phase impurities on recrystallized grain size depends on various factors such as the type, concentration, distribution, and interaction of the impurities with the host material. Second-phase impurities can act as pinning sites for the migrating grain boundaries during recrystallization. As a result, the movement of these boundaries is hindered, leading to a finer grain size. This pinning effect is particularly evident when the impurities are finely dispersed throughout the material. The tectonically deformed samples show a clear trend of decreasing grain size with increasing impurity content (Figure 16) which is not visible for the creep-tested samples.

Overall, no substantiated correlation was found between the measured creep rates and the investigated microstructural parameters. This could relate to the relatively short runtime for the individual load steps, in which steady-state was not reached. In Figure 17, we plot the strain rates related to the different load steps against the different parameters: the initial and the post mortem grain size, the grain size refinement factor, the initial mega-grain content, and the second phase content, and use linear regression to identify potential connections. In the vast majority, no correlation was found. Taking into account the relatively small number of samples compared to a large number of expected influencing parameters, which also include parameters that were not measured in this study, such as the water content, parameters that yield some correlation with the strain rate ($R^2 > 0.2$) will be discussed in the following. Regarding the grain size, a small correlation of strain rate with the grain size of the tectonically deformed samples was found for the 3 MPa and 4 MPa load steps, showing a trend of decreasing strain rate with increasing grain size, which would be expected in the case of creep by grain size-sensitive pressure solution (Figure 17a). The same trend is visible for the grain size of the lab-deformed samples for the 5 MPa load step (Figure 17b). Grain size seems not to affect the creep behaviour in the dislocation creep regime at the higher load steps, in agreement with the grain size-insensitive creep behaviour. The mega-grain content does not seem to influence the strain rate for the different load steps (Figure 17d). For all load steps we observe a trend of decreasing strain rate with increasing second phase content (Figure 6 and Figure 17e), for both, the higher-stress dislocation creep and the lower-stress pressure solution creep regimes.

The weak correlation of the strain rates with the microstructural parameters is thought to be caused by the small number of data points in relation to the high variability of the natural salt and the short duration of the experiments. Further, the different strain paths, caused by varied load steps in between the creep tests, may have resulted in varying amounts of strain localization and subsequent recrystallization.

Table 3. Grain size statistics lab-deformed samples.

	d [mm]							Ln d						
Thin section ID	Number of grains	Min [mm]	Max [mm]	Median [mm]	Average [mm]	Std_deviation [mm]	Mode [mm]	Number of grains	Min	Max	Median	Average	Std_deviation	Mode
ZW_MaP_17_pre	496	0.04	5.27	0.41	0.75	0.88	0.14	496	-3.15	1.66	-0.89	-0.79	1.00	-1.98
ZW_MaP_18_pre	783	0.02	7.03	0.33	0.61	0.86	0.28	783	-3.98	1.95	-1.10	-1.04	1.00	-1.28
ZW_MaP_19_pre	593	0.03	9.44	0.29	0.53	0.86	0.52	593	-3.60	2.25	-1.23	-1.19	1.00	-0.66
ZW_MaP_34_d	502	0.05	5.47	0.41	0.61	0.60	1.08	502	-3.09	1.70	-0.88	-0.84	0.82	0.08
ZW_MaP_35_d	500	0.05	6.22	0.62	0.85	0.73	0.61	500	-2.99	1.83	-0.48	-0.52	0.89	-0.49
ZW_MaP_36_d	502	0.08	5.47	0.63	0.87	0.78	1.11	502	-2.58	1.70	-0.46	-0.46	0.80	0.11
ZW_MaP_37_d	506	0.04	3.83	0.59	0.74	0.58	0.53	506	-3.32	1.34	-0.53	-0.57	0.76	-0.64
ZW_MaP_38_d	506	0.07	4.88	0.68	0.89	0.72	1.01	506	-2.67	1.58	-0.38	-0.42	0.81	0.01
ZW_MaP_39_d	409	0.03	14.97	0.74	1.28	1.70	2.28	409	-3.50	2.71	-0.30	-0.29	1.01	0.83
ZW_MaP_44_d	2830	0.01	13.80	0.46	0.81	0.96	0.09	2830	-4.51	2.62	-0.77	-0.78	1.11	-2.37
ZW_Map_45_d	2635	0.01	9.20	0.39	0.63	0.78	0.01	2635	-4.58	2.22	-0.94	-0.97	1.05	-4.35
ZW_Map_46_d	1908	0.01	7.49	0.39	0.64	0.78	0.03	1908	-4.58	2.01	-0.94	-0.99	1.11	-3.67
ZW_Map_47_d	1437	0.01	11.33	0.46	0.87	1.18	0.01	1437	-4.58	2.43	-0.78	-0.77	1.17	-4.31
ZW_Map_48_d	561	0.04	6.53	0.49	0.72	0.72	0.27	561	-3.10	1.88	-0.71	-0.68	0.82	-1.32
ZW_Map_49_d	1256	0.01	6.13	0.30	0.51	0.63	0.02	1256	-4.58	1.81	-1.19	-1.27	1.18	-4.16

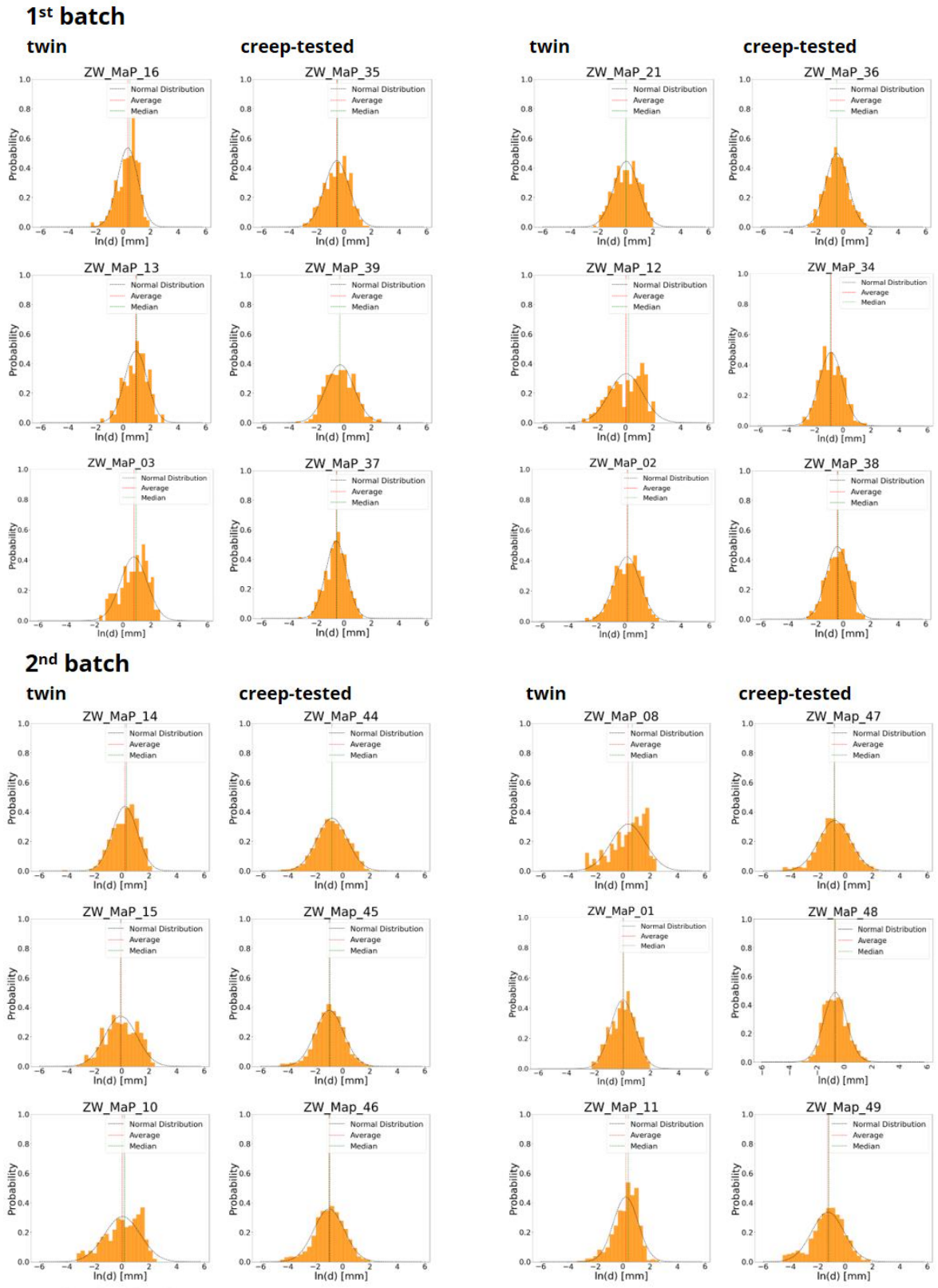

Figure 14. Histograms show the grain size distribution of the tectonically-deformed samples on the left, juxtaposed with the creep-tested samples on the right. For additional details on the grain size statistics, refer to the accompanying text, Table 2 and Table 3, and consult Appendix A for information on grain size measurements.

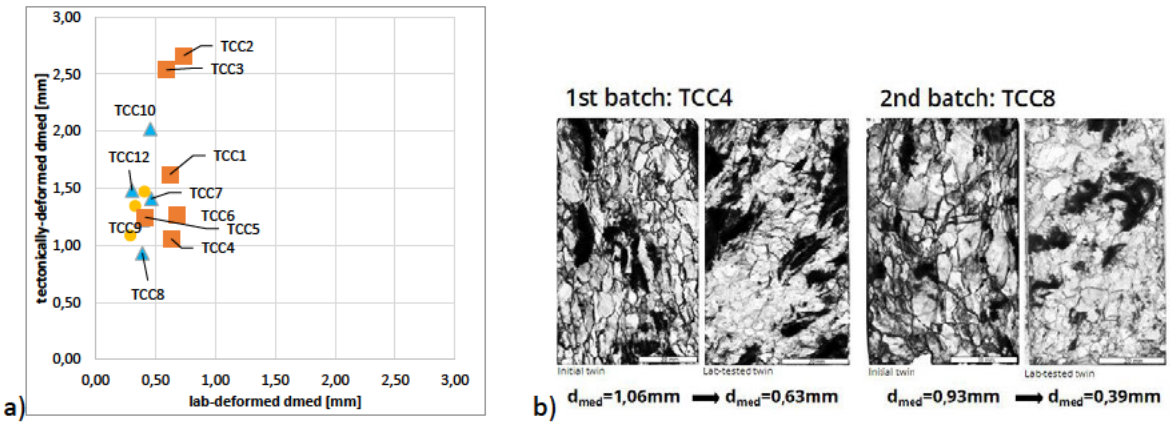

Figure 15. a) Graph depicts the recrystallized grain size of the tectonically deformed samples compared to the grain size of the lab-deformed twins, orange symbols = 1st batch, blue symbols = 2nd batch, yellow symbols = pre-tests ; b) transmitted light micrographs juxtaposing twin samples before and after the creep-tests, representing the 1st sample batch to the left and the 2nd sample batch to the right. Refer to the accompanying text for detailed explanations.

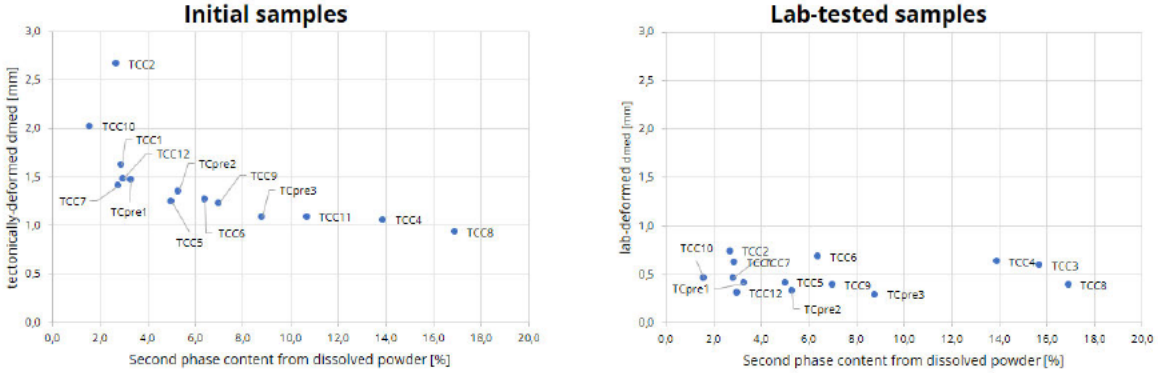

Figure 16. Graphs show the tectonically recrystallized grain size as a function of the impurity content (left) and the grain size of the creep-tested samples as a function of the impurity content (right).

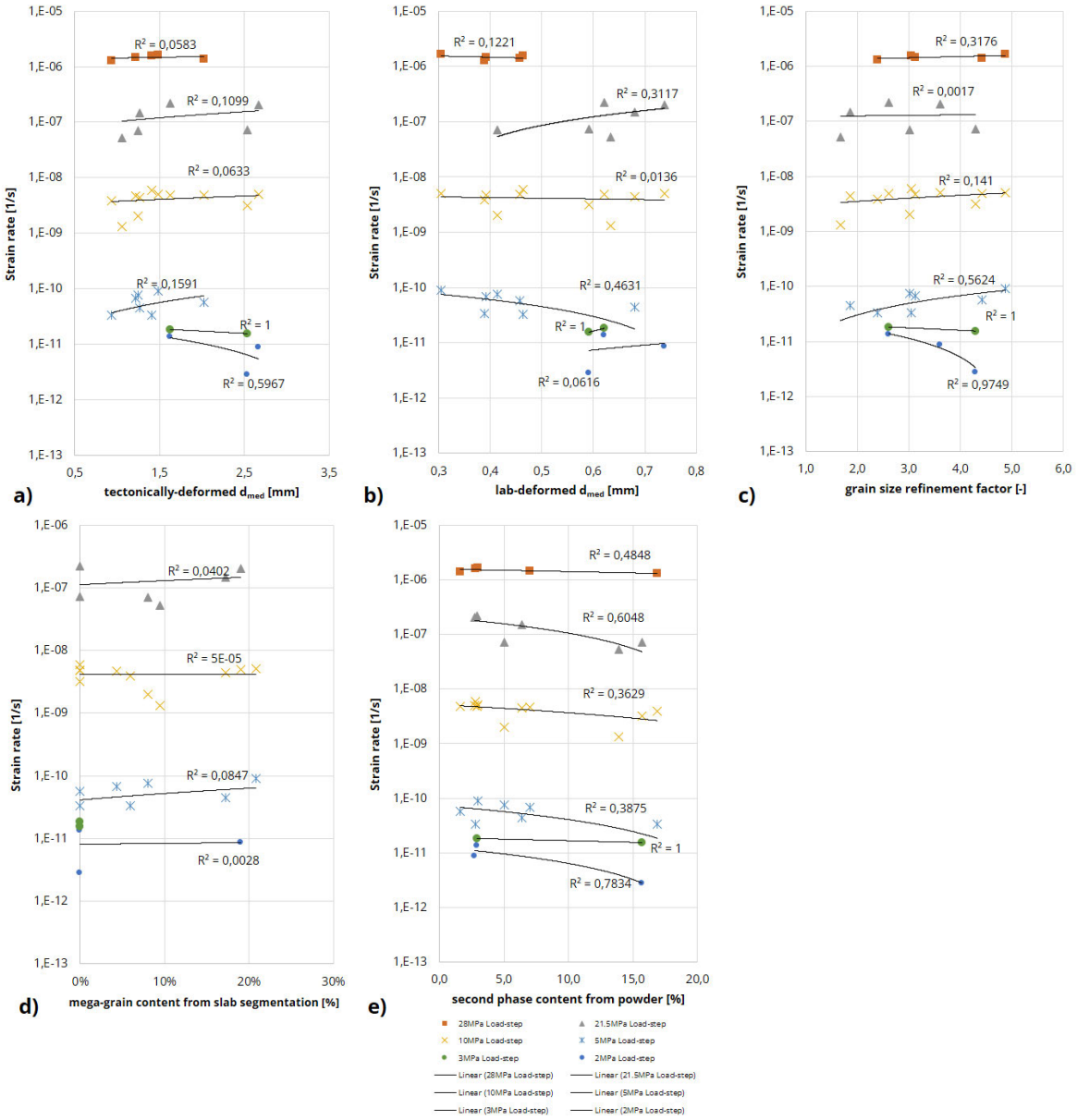

Figure 17. Graphs display the strain-rates of the 11 creep-tested samples (Figure 1) in relation to: a) the matrix grain size of the tectonically deformed samples, b) the post-mortem matrix grain size of creep-tested samples, c) the grain size refinement factor, d) the mega-grain content derived from slab segmentation, and e) the second phase content derived from dissolved powder. Refer to the accompanying text for detailed explanations.

4.3.2.3 Subgrain size

In the samples we measure subgrains of variable size and shape (Figure 18), suggesting different stress loads or tectonic deformation events. The presence of small subgrains may indicate areas where the high differential stress has been recorded, possibly as a result of localized deformation or strain. Conversely, the larger subgrains could be related to the lower stress load steps or are preserved from the initial sample state and represent tectonic deformation.

In total, 4248 subgrains were measured in the tectonically deformed twins, and 3678 were measured for the creep-tested samples. The average of the average grain size for the tectonically-deformed twins is 129 µm (n=9, min= 83 µm, max= 1458 µm, Std.Dev= 23 µm, see Table 4), and 56 µm for the creep-tested samples (n=12, min= 22 µm, max= 144 µm, Std.Dev= 32 µm, Table 4).

The average subgrain size of the creep-tested samples is significantly smaller than the subgrain size of the tectonically deformed samples, and the average subgrain size of both the tectonically deformed

samples and the creep-tested samples aligns well with the calibrated piezometer by Carter et al. (1993, refer to Figure 19). For the creep-tested samples the piezometer suggests and a maximum differential stress in the range of 4 MPa, which could represent the last load steps at lower differential stress, though the pronounced variability of the subgrain size related to different measured areas within one sample in the creep-tested samples suggest that the average subgrain size represents preserved stages of the different load steps and that steady-state was not reached.

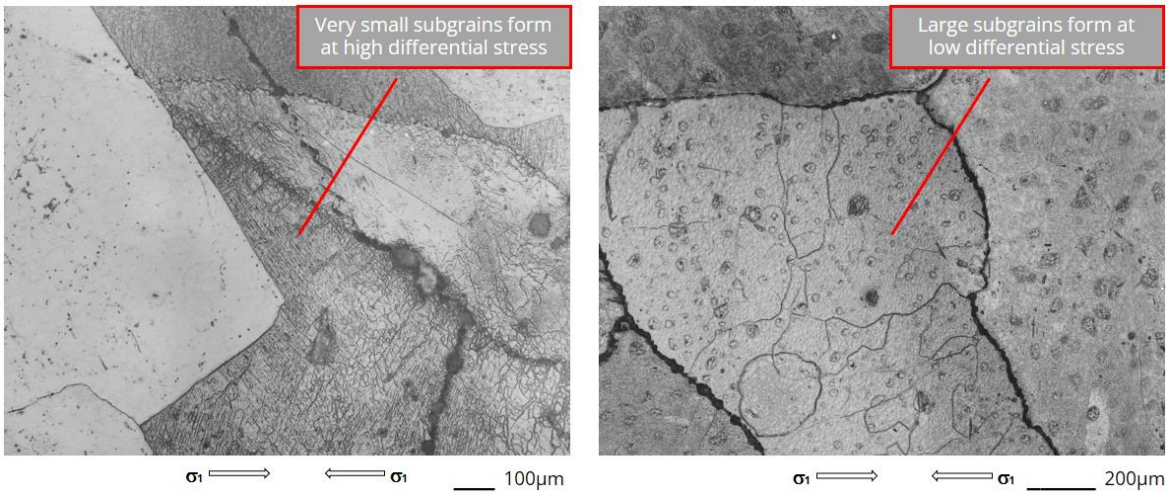

Figure 18. Reflected light micrographs showing subgrains of variable size and shape.

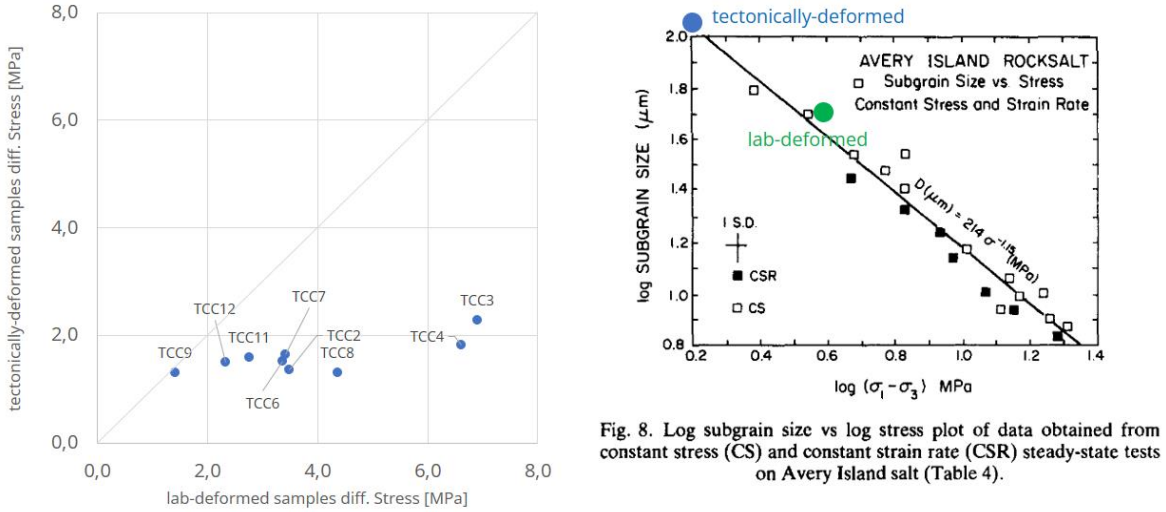

Figure 19. Graphs showing (left) derived differential stress of the tectonically-deformed samples vs. the lab-deformed samples. Right: Correlation of subgrain size with differential stress from Carter et al., 1993.

Table 4 SGSD before and after creep-testing

Twin MaP ID (ZW1.1)	Number of grains	Average [µm]	Std_deviation [µm]	D/214 [µm]	diff. Stress [MPa]	log (D)	log (diff. Stress)	IfG lab lest ID	MaP ID	Number of grains	Average [µm]	Std_deviation [µm]	D/214 [µm]	diff. Stress [MPa]	log (D)	log (diff. Stress)
ZW_MaP_16	-	-	-	-	-	-	-	TCC1	ZW_MaP_35_d	310	49	54	0.2	3.6	1.7	0.6
ZW_MaP_13	499	149	126	0.7	1.4	2.2	0.1	TCC2	ZW_MaP_39_d	301	51	35	0.2	3.5	1.7	0.5
ZW_MaP_03_g	307	83	93	0.4	2.3	1.9	0.4	TCC3	ZW_MaP_37_d	302	23	40	0.1	6.9	1.4	0.8
ZW_MaP_21	137	107	106	0.5	1.8	2.0	0.3	TCC4	ZW_MaP_36_d	304	24	28	0.1	6.6	1.4	0.8
ZW_MaP_12	-	-	-	-	-	-	-	TCC5	ZW_MaP_34_d	302	22	14	0.1	7.2	1.3	0.9
ZW_MaP_02_g	505	132	112	0.6	1.5	2.1	0.2	TCC6	ZW_MaP_38_d	308	53	61	0.2	3.4	1.7	0.5
ZW_MaP_14	218	120	113	0.6	1.6	2.1	0.2	TCC7	ZW_MaP_44_d	311	52	51	0.2	3.4	1.7	0.5
ZW_MaP_15	472	158	167	0.7	1.3	2.2	0.1	TCC8	ZW_MaP_45_d	333	39	40	0.2	4.4	1.6	0.6
ZW_MaP_10	328	156	142	0.7	1.3	2.2	0.1	TCC9	ZW_MaP_46_d	302	144	132	0.7	1.4	2.2	0.1
ZW_MaP_08	-	-	-	-	-	-	-	TCC10	ZW_MaP_47_d	302	66	71	0.3	2.8	1.8	0.4
ZW_MaP_01_g	498	125	103	0.6	1.6	2.1	0.2	TCC11	ZW_MaP_48_d	300	67	56	0.3	2.8	1.8	0.4
ZW_MAP_11	1284	134	122	0.6	1.5	2.1	0.2	TCC12	ZW_MAP_49_d	303	81	63	0.4	2.3	1.9	0.4

5 Summarizing remarks

This work package focuses on characterizing and analysing the microstructural properties of Zuidwending salt samples subjected to deformation experiments. The primary objectives include understanding the influence of deformation mechanisms, grain size, and impurity content on the salt's creep behaviour. The analysis addresses both laboratory experiments and comparisons with tectonically-deformed samples.

During the pre-tests, conducted to aid in the planning of the comprehensive creep tests, the texture of Zuidwending salt characterized by halite mega-grains and a matrix of fine- to coarse-grained halite is preserved. Dynamic recrystallization is evident, resulting in the creation of new, smaller grains that substitute approximately 25 area% of the initial matrix grains.

Creep tests conducted with decreasing load steps stress result in significant alterations to the initial texture, including a reduction in matrix and mega-grain sizes. Mega-grains transform into coarse-grained polycrystals, displaying strain-induced distortion. Grain boundary processes, including fluid inclusion patterns, serrated boundaries, and efflorescence, are examined in detail. Grain size measurements, indicate a significant decrease of the grain size during creep tests, with no substantial correlation found between grain size with the observed creep rates. It was found that an increasing impurity content could be related to a decreasing strain rate for both the dislocation creep and the pressure solution creep regime. Subgrain size analysis serves as a piezometer, suggesting higher stresses during creep tests compared to tectonically-deformed samples.

While the complexity of the relationship between grain size, impurity content, and creep behaviour requires further exploration, this study contributes valuable insights into the intricate interplay of microstructural elements in Zuidwending salt subjected to deformation. The main findings of the study are listed in Table 5.

Table 5 Overview results, interpretation, and interrelation to other work packages.

Task ZW2.1	Result ZW2.2	linked work packages
Microstructural investigation and comparison with microstructure prior to creep tests (ZW1.2) (texture, grain boundary structure, microstructural processes, rheology)	**Texture:** Dynamically recrystallized fabric. **Grain boundary structure**: Overall tight grain boundaries with (semi)-connected fluid films **Microstructural processes:** Mega-grain refinement is attributed to progressive strain-induced distortion of the crystal lattice; Matrix grains are dynamically recrystallized with overall decreased grain size **Rheology:** Dislocation creep at high deviatoric stress and pressure solution creep at low deviatoric stress.	*Input work packages:* **ZW1.1** Selection of representative or typical core pieces for microscale analyses, integrated with deformation and permeation experiments **ZW1.2**: Microstructure and microchemistry of undeformed selected samples **ZW2.2**: Design, supervision, and analysis of deformation experiments at IfG *Direct output in work packages:* **ZW2.4**: Determine feasible limits of stress and strain rates in the low stress/low strain rate regime **ZW2.6**: Determine a site-specific constitutive model that is adapted to the local requirements **ZW4.1**: Model for constitutive law in salt surrounding the cavern
Grain size measurement and comparison with grain size distribution prior to creep tests (ZW1.2).	Median grain size after the creep tests: 0.44 mm (Std.Dev 0.16 mm), tectonically deformed twins have a median grain size of 1.49 mm (Std.Dev 1.26 mm)	
Study on the effect of microstructural parameters on strain rate	Overall, no substantiated correlation was found between the measured creep rates and the investigated microstructural parameters. The observed decrease in strain rates with increasing second phase content suggests that grain boundary pinning is influencing the rheology of the natural rock salt.	